Inside the Stagnation Radius of the Nearest Billion-Solar-Mass Black Hole

J. M. Wrobel,[1] D. W. Pesce,[2, 3] and K. E. Nyland[4]

[1] National Radio Astronomy Observatory, P.O. Box O, Socorro, NM 87801, USA

[2] Center for Astrophysics | Harvard & Smithsonian, 60 Garden Street, Cambridge, MA 02138, USA

[3] Black Hole Initiative, Harvard University, 20 Garden Street, Cambridge, MA 02138, USA

[4] U.S. Naval Research Laboratory, 4555 Overlook Ave SW, Washington, DC 20375, USA

ABSTRACT

We used the NSF Jansky Very Large Array at a frequency $\nu = 22\,\mathrm{GHz}$ to study the nearest billion-solar-mass black hole, in the early-type galaxy NGC 3115 at a distance of 9.7 Mpc. We localize a faint continuum nucleus, with flux density $S_{22\,\mathrm{GHz}} = 48.2 \pm 6.4\,\mu\mathrm{Jy}$, to a FWHM diameter $d_{22\,\mathrm{GHz}} < 59\,\mathrm{mas}$ (2.8 pc). We find no evidence for adjacent emission within a stagnation region of radius $R_{\mathrm{sta}} \sim 360\,\mathrm{mas}$ (17 pc) identified in a recent hydrodynamic simulation tailored to NGC 3115. Within that region, the simulated gas flow developed into an advection-dominated accretion flow (ADAF). The nucleus' luminosity density $L_{22\,\mathrm{GHz}} = 5.4 \times 10^{17}\,\mathrm{W\,Hz^{-1}}$ is about 60 times that of Sagittarius A*. The nucleus' spectral index $\alpha_{10\,\mathrm{GHz}}^{22\,\mathrm{GHz}} = -1.85 \pm 0.18$ ($S_\nu \propto \nu^\alpha$) indicates optically-thin synchrotron emission. The spectral energy distribution of the nucleus peaks near $\nu_{\mathrm{peak}} = 9\,\mathrm{GHz}$. Modeling this radio peak as an ADAF implies a black hole mass $M_{\mathrm{ADAF}} = (1.2 \pm 0.2) \times 10^9\,M_\odot$, consistent with previous estimates of $(1-2) \times 10^9\,M_\odot$ from stellar or hot-gas dynamics. Also, the Eddington-scaled accretion rate for NGC 3115, $\dot{M}_{\mathrm{ADAF}}/\dot{M}_{\mathrm{Edd}} = 1.2^{+1.0}_{-0.6} \times 10^{-8}$, is about 4-8 times lower than recent estimates for Sagittarius A*.

1. MOTIVATION

Supermassive black holes (BHs) spend the majority of their time accreting at well below the Eddington rate $\dot{M}_{\mathrm{Edd}} = 2.2 \times 10^{-8}\,M\,M_\odot\,yr^{-1}$, where M is the BH mass in Solar units (e.g., Heckman & Best 2014). In the local Universe this accretion state manifests as low-luminosity active galactic nuclei (LLAGNs; e.g., Ho 2008, 2009). For LLAGNs, it is thought that the material near the BHs follows the advection-dominated accretion flow (ADAF) solution to the hydrodynamic equations for viscous and differentially rotating flows (e.g., Yuan & Narayan 2014). Direct imaging of such accretion flows is beyond current observational capabilities and strongly motivates the design of future facilities, such as the next-generation Event Horizon Telescope (ngEHT; Johnson et al. 2023; Doeleman et al. 2023; Nair et al. 2024).

Further from the BHs, the ADAFs may be fed by Bondi accretion from the hot atmospheres of their host spheroids (e.g., Yuan & Narayan 2014). In a few cases X-ray facilities can spatially resolve the Bondi regions (e.g., Inayoshi et al. 2020), informing theoretical studies of how the gas densities (ρ), temperatures, and accretion rates ($\dot{M}$) vary with radius R from the BH (e.g., Inayoshi et al. 2018; Cho et al. 2023; Guo et al. 2023). For example, a measured $\rho(R)$ can be compared with $\rho(R) \propto R^{-1.5}$ from Bondi theory. Profiles flatter than Bondi may suggest that the accretion flows are directing some of their mass away from the BHs and suppressing their ability to radiate – the hallmark of LLAGNs.

Such generic comparisons can provide guidance about accretion flow suppression. But stronger insights will follow from realistic calculations or simulations that are tailored to the unique settings of individual LLAGNs, such as accretion onto Sagittarius A* via the stellar winds of nearby Wolf-Rayet stars (e.g., Ressler et al. 2018).

Corresponding author: J. M. Wrobel
Email: jwrobel@nrao.edu

Here, we focus on NGC 3115 at a distance $D = 9.7\,\mathrm{Mpc}$ (Tonry et al. 2001) as it hosts the nearest billion-solar-mass BH, with a fiducial mass $M_{\mathrm{fid}} \sim 1.5 \times 10^9\,M_\odot$ from stellar or hot-gas dynamics (Kormendy et al. 1996; Emsellem et al. 1999; Wong et al. 2011, 2014). The LLAGN of this early-type galaxy (ETG) was discovered with the NSF Very Large Array (VLA; Thompson et al. 1980) in its A configuration at a frequency $\nu = 8.5\,\mathrm{GHz}$ (Wrobel & Nyland 2012). It has a flux density $S_{8.5\,\mathrm{GHz}} = 290 \pm 30\,\mu\mathrm{Jy}$ (corresponding to a luminosity density $L_{8.5\,\mathrm{GHz}} = 3.3 \times 10^{18}\,\mathrm{W\,Hz^{-1}}$ or $L_{8.5\,\mathrm{GHz}} = 3.3 \times 10^{25}\,\mathrm{erg\,s^{-1}\,Hz^{-1}}$) and a diameter $d_{8.5\,\mathrm{GHz}} < 170\,\mathrm{mas}$ (8.0 pc). For context at 8.5 GHz, Krajnović & Jaffe (2002) and Capetti et al. (2009) used the VLA in its A configuration to search for LLAGN in dozens of optically selected ETGs, but their detection thresholds precluded discovery of analogs of the LLAGN in NGC 3115.

Confusion from NGC 3115's population of X-ray binaries means that the LLAGN cannot be assigned a counterpart at 2-10 keV (Wrobel & Nyland 2012; Wong et al. 2014). This implies an X-ray-to-Eddington ratio of less than 2.1×10^{-9} assuming a radiative efficiency $\eta = 0.1$ for the Eddington luminosity. Applying the Ho (2009) bolometric correction leads to a bolometric-to-Eddington ratio $L_{\mathrm{bol}}/L_{\mathrm{Edd}} < 3.3 \times 10^{-8}$, an extreme ratio rare among LLAGNs in optically selected galaxies. NGC 3115's LLAGN also lacks evidence for optical emission lines like $H\alpha$, $H\beta$, and O III (Ho et al. 2003; Guérou et al. 2016). Such galaxies are referred to as having absorption-line or passive nuclei (Ho et al. 2003; Nyland et al. 2016).

The fiducial M_{fid} and the hot-atmosphere sound speed (Wong et al. 2011, 2014) for NGC 3115 imply a Bondi radius $R_{\mathrm{Bon}} = 3\farcs6$ (170 pc). Yao & Gan (2020) performed 2D hydrodynamic simulations of gas flows tailored to NGC 3115's well-studied traits within $5\,R_{\mathrm{Bon}}$. They identified a stagnation region of radius $R_{\mathrm{sta}} \sim 0.1\,R_{\mathrm{Bon}} \sim 360\,\mathrm{mas}$ (17 pc): the dominant gas motions were inflows inside R_{sta} and outflows beyond R_{sta}. 1D calculations also tailored to NGC 3115 identified a similar stagnation region (Shcherbakov et al. 2014). Inside R_{sta} the Yao & Gan (2020) simulation developed two ADAF traits, namely gas densities that varied with radius R as $\rho(R) \propto R^{-0.8}$ and a geometrically-thick disk containing hot electrons and hotter ions. The accretion also mainly occurred within the polar regions, a trait also recognized in a tailored 3D hydrodynamic simulation of Sagittarius A* (Ressler et al. 2018). Yao & Gan (2020) did not consider magnetic fields, so the emissive properties of their simulated ADAF cannot be compared to the LLAGN (Wrobel & Nyland 2012).

But that the simulation developed an ADAF does motivate another approach to studying NGC 3115: assemble the LLAGN's spectral energy distribution (SED) and model it using ADAF theory (e.g., Narayan & Yi 1995a,b; Mahadevan 1997; Nemmen et al. 2014; Bandyopadhyay et al. 2019; Pesce et al. 2021). It might be that both the outflow-dominated and inflow-dominated regions are emitting. Our focus is on the SED of the latter. To mitigate contamination from emission beyond R_{sta}, the SED should ideally be assembled at high resolutions, taken to mean resolutions at full width half maximum (FWHM) of less than $2R_{\mathrm{sta}} \sim 720\,\mathrm{mas}$ (34 pc).

Almeida et al. (2018) pioneered the SED approach for NGC 3115, but had only one radio detection of the LLAGN at a high resolution (Wrobel & Nyland 2012). The Yao & Gan (2020) simulation guides us to seek more detections of the LLAGN at high resolution ($< 2R_{\mathrm{sta}}$) and to treat data at low resolution ($> 2R_{\mathrm{sta}}$) as upper limits on the LLAGN. In Section 2 of this paper, we report a new, high-resolution radio detection of the LLAGN in NGC 3115. In Section 3 we use the new and literature data to better define the properties of the LLAGN inside R_{sta}. We also briefly touch on conditions beyond R_{sta} in Section 4. We close, in Section 5, with a summary and conclusions.

Throughout, uncertainties are reported as 1σ unless stated otherwise and literature distances are converted to $D = 9.7\,\mathrm{Mpc}$ (Tonry et al. 2001) when necessary.

2. DATA

NGC 3115 was observed on 2024 December 19 and 20 UT with the A configuration of the NSF Karl G. Jansky Very Large Array (JVLA; Perley et al. 2011). A coordinate equinox of 2000 was employed. J1007−0207, at a position $\alpha(J2000) = 10^h07^m04\fs34992$, $\delta(J2000) = -02°07'10\farcs9177$ and with a 1D position error of 2.0 mas, was used as a gain calibrator. The switching time between it and NGC 3115 was 4 m and involved a switching angle of 5.6°. Reference pointing was implemented.

Data were acquired in dual circular polarizations, each spanning $4 \times 2\,\mathrm{GHz}$ of bandwidth centered at $\nu = 22\,\mathrm{GHz}$. 3C 286 was observed to set the amplitude scale to an estimated accuracy of 10%. This estimate stems from the modest elevation differences of 9-16° between observations of 3C 286 and the gain calibrator, and conservatively doubles the base level suggested by Perley & Butler (2017). The exposure time on NGC 3115 was about 1.5 h per observation. Polarization calibration was not implemented, as each day's observation spanned only a few hours.

The visibility data were pipeline calibrated and custom imaged using versions 6.6.1 and 6.6.4-34, respec-
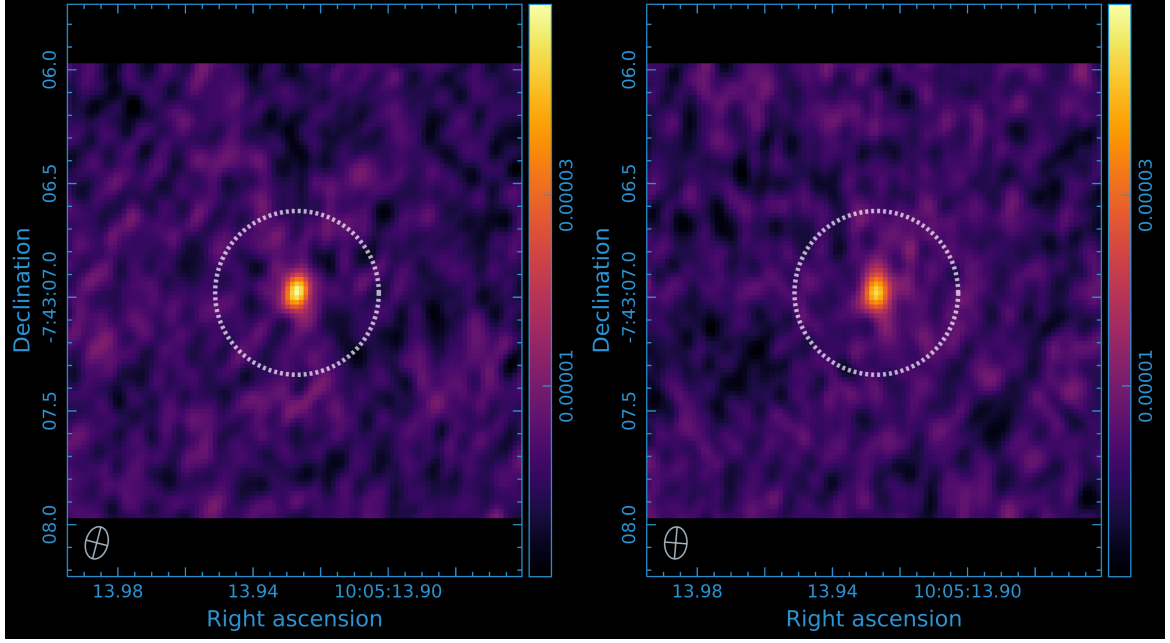
Figure 1. JVLA images of the Stokes I emission at $\nu = 22\,\text{GHz}$ from NGC 3115, visualized via The Cube Analysis and Rendering Tool for Astronomy (CARTA; Comrie et al. 2021). The scale is $1'' = 47\,\text{pc}$. The ellipses show the synthesized beam dimensions at FWHM, characterized by their major axes θ_{maj}, minor axes θ_{min}, and elongation position angles. The ellipses share the same geometric angular resolution $\theta_{\text{geo}}^{22\,\text{GHz}} = \sqrt{\theta_{\text{maj}} \times \theta_{\text{min}}} = 120\,\text{mas}$ (5.6 pc). The dashed circle shows the stagnation region diameter $2R_{\text{sta}}$ from the Yao & Gan (2020) simulation. The color bar linearly spans -10 to $+50\,\mu\text{Jy beam}^{-1}$. Left: UT date is 2024 December 19. Root-mean-square (RMS) noise is $3.0\,\mu\text{Jy beam}^{-1}$. Right: UT date is 2024 December 20. RMS noise is $3.2\,\mu\text{Jy beam}^{-1}$.

tively, of the Common Astronomy Software Applications package (CASA Team et al. 2022). For each observation, task `tclean` was used to form an image of the Stokes I emission from NGC 3115 by weighting the visibility data with a Briggs robustness of 0.5 and invoking the mtfs deconvolver with a straight-line spectral model (Figure 1). The images spanned 100 pixels per axis and had 20 mas pixels. Each image independently detects the nucleus at $\nu = 22\,\text{GHz}$ and locates its peak at a position $\alpha(J2000) = 10^h05^m13\overset{s}{.}927$, $\delta(J2000) = -07°43'06''\!.98$. The position error is dominated by phase-referencing strategies and a 1D estimate for it is about 100 mas.

We combined the calibrated visibility data from both observations at $\nu = 22\,\text{GHz}$ and jointly fit models to them, assuming no changes in the source between the two observations (Figure 2). (The source size modeling procedure is detailed in Appendix A.) A Gaussian source model for the nucleus' flux density found it to be (1) faint, with $S_{22\,\text{GHz}} = 48.2 \pm 6.4\,\mu\text{Jy}$, where the error is the quadratic sum of the modeling uncertainty and the 10% amplitude-scale uncertainty; and (2) point-like, with a FWHM diameter $d_{22\,\text{GHz}} < 59\,\text{mas}$ (99.7% confidence region). A linear model for the nucleus' in-band spectral index found $\alpha_{18\,\text{GHz}}^{26\,\text{GHz}} = -2.3 \pm 0.7$ ($S_\nu \propto \nu^\alpha$), broadly indicating a synchrotron origin. The large error in $\alpha_{18\,\text{GHz}}^{26\,\text{GHz}}$ is mainly due to the source's limited signal-to-

noise ratio. The above modeling results, rather than the images in Figure 1, will be used hereafter to characterize the nucleus.

With adequate signal-to-noise, structures as large as $1''\!.2$ could be represented at $\nu = 22\,\text{GHz}$. But no such structures were found after tapering the visibility data to achieve $\theta_{\text{geo}}^{22\,\text{GHz}} = 300\,\text{mas}$ and $520\,\text{mas}$, with off-nuclear RMS noise levels of $4.9\,\mu\text{Jy beam}^{-1}$ and $6.9\,\mu\text{Jy beam}^{-1}$, respectively. Also, the nuclear flux densities from the tapered images agreed with the $S_{22\,\text{GHz}}$ inferred from the Gaussian source model.

Table 1 augments the new $S_{22\,\text{GHz}}$ with previous continuum photometry for NGC 3115 at lower radio frequencies, including 3σ upper limits at low resolution $\theta_{\text{geo}}^\nu > 2R_{\text{sta}}$ and detections at high resolution $\theta_{\text{geo}}^\nu < 2R_{\text{sta}}$. Figure 3 shows the resulting broadband spectrum. The nucleus has a band-to-band spectral index $\alpha_{10\,\text{GHz}}^{22\,\text{GHz}} = -1.85 \pm 0.18$, indicating optically-thin synchrotron emission and reinforcing the synchrotron origin suggested from the in-band's $\alpha_{18\,\text{GHz}}^{26\,\text{GHz}} = -2.3 \pm 0.7$ (Figure 2).

3. INSIDE THE STAGNATION RADIUS

Adopting a distance $D = 9.7\,\text{Mpc}$ for NGC 3115 (Tonry et al. 2001), $1''$ subtends 47 pc. Gas motions are predominantly inflows inside the stagnation radius

Table 1. Photometry for NGC 3115's Broadband Spectrum

UT Date	Frequency ν (GHz)	Resolution $\theta_{\rm geo}^{\nu}$ (mas)	Resolution $\theta_{\rm geo}^{\nu}$ (pc)	Local RMS μJy beam^{-1}	Flux Density S_{ν} (μJy)	Luminosity Density L_{ν} (W Hz^{-1})	Ref.
(1)	(2)	(3)	(4)	(5)	(6)	(7)	
2002 Aug 12	1.4	5900	280	150	< 450	$< 5.1 \times 10^{18}$	1
2021 Dec 14	3.0	2800	130	130	< 390	$< 4.4 \times 10^{18}$	2
1987 Feb 1	4.9	8500	400	110	< 330	$< 3.7 \times 10^{18}$	3
2004 Nov 16	8.5	300	14	18	290 ± 30	3.3×10^{18}	4
2015 Jun 12	10	240	11	4.4	207 ± 10	2.3×10^{18}	5
2024 Dec 19-20	22	120	5.6	3.1	48.2 ± 6.4	5.4×10^{17}	6

NOTE—References. (1) White et al. (1997); (2) Lacy et al. (2020); (3) Fabbiano et al. (1989); (4) Wrobel & Nyland (2012); (5) Jones et al. (2019); (6) this work.
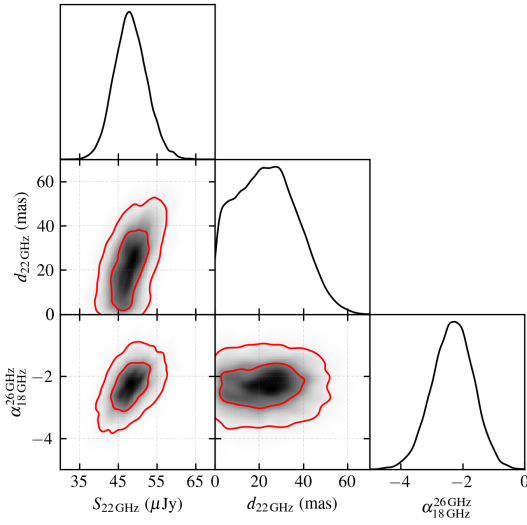
Figure 2. Posterior distribution of a circular Gaussian's flux density $S_{22\,\rm GHz}$, FWHM diameter $d_{22\,\rm GHz}$, and a linear model for the in-band spectral index $\alpha_{18\,\rm GHz}^{26\,\rm GHz}$. Inner and outer contours enclose probabilities of 50% and 90%, respectively.

Figure 3. Broadband spectrum of the LLAGN in NGC 3115. Triangles indicate 3σ upper limits with $\theta_{\rm geo}^{\nu} > 2R_{\rm sta}$. Circles with 1σ error bars indicate detections with $\theta_{\rm geo}^{\nu} < 2R_{\rm sta}$. The faint gray lines are individual samples from the posterior distribution, which illustrate the full range of model behavior. The thick black line shows the posterior average, which is a fit to the thermal ADAF model presented in Section 3.3.

$R_{\rm sta} \sim 360\,{\rm mas}$ (17 pc) identified in the simulation tailored to NGC 3115 (Yao & Gan 2020).

3.1. *Physical Traits*

NGC 3115's point-like continuum nucleus – its LLAGN – is localized to a FWHM diameter $d_{22\,\rm GHz} < 59\,{\rm mas}$ (2.8 pc). This is three times smaller than previous localizations based on images near 9 GHz (Wrobel & Nyland 2012; Jones et al. 2019). Assuming that the LLAGN at $\nu = 22\,{\rm GHz}$ coincides with the BH, the localization radius corresponds to less than 10^4 times the Schwarzschild radius $R_{\rm Sch} = 2GM_{\rm fid}/c^2$ of the fiducial BH mass $M_{\rm fid} \sim 1.5 \times 10^9\,M_{\odot}$. The FWHM diame-

ter and flux density of the LLAGN imply a brightness temperature higher than 240 K at $\nu = 22\,{\rm GHz}$.

The position of the LLAGN at $\nu = 22\,{\rm GHz}$ agrees to within 50 mas with those reported near $\nu = 9\,{\rm GHz}$ (Wrobel & Nyland 2012; Jones et al. 2019), which in turn coincide with the position of the galaxy's photocenter measured in the infrared K-band (Skrutskie et al. 2006; Jones et al. 2019). In the optical V-band the stellar nucleus of NGC 3115 is spatially resolved and has a half-light diameter $d_{\rm hal} = 108\,{\rm mas}$ (5.1 pc; Kormendy et al. 1996; Emsellem et al. 1999). The 1D calculations and

the 2D hydrodynamic simulations tailored to NGC 3115 assume that the BH is centered on the stellar nucleus (Shcherbakov et al. 2014; Yao & Gan 2020). But the positional accuracy of the stellar nucleus ($\pm$ 500 mas at 95% confidence; Norris et al. 2014) is insufficient to say if it coincides with the LLAGN.

The LLAGN appears to be isolated at $\nu = 22$ GHz, with no evidence for off-nuclear emission on scales from 120 mas (5.6 pc) to $1''2$ (56 pc). This range fully samples the diameter $2R_{st} \sim 720$ mas (34 pc) of the stagnation region identified in the Yao & Gan (2020) simulation, where the dominant gas motions are inflows. Isolation of the LLAGN was also noted from moderately deep images near $\nu = 9$ GHz with high resolution, $\theta^\nu_{geo} < 2R_{sta}$ (Table 1).

NGC 3115's LLAGN has a steep spectrum indicative of synchrotron emission, measured in-band $\alpha^{26\,GHz}_{18\,GHz} = -2.3 \pm 0.7$ and band-to-band $\alpha^{22\,GHz}_{10\,GHz} = -1.85 \pm 0.18$. The latter statement assumes flux density stability between 9.5 yr, a trait previously found to hold near $\nu = 9$ GHz between 10.6 yr (Jones et al. 2019). Still, if the band-to-band index is compromised by time variability, then much of the radiating material would need to occupy a volume, set by light travel times, of diameter $\lesssim 19$ light yr (5.8 pc). Such an upper limit would be consistent with the measured diameter $d_{22\,GHz} < 59$ mas (2.8 pc) and further underscore the compactness of the LLAGN.

At $\nu = 22$ GHz, NGC 3115's synchrotron nucleus has a luminosity density $L_{22\,GHz} = 5.4 \times 10^{17}$ W Hz^{-1}. This is only about 60 times that of Sagittarius A*, which has a distance $D = 8.1$ kpc (Reid et al. 2019; GRAVITY Collaboration et al. 2019) and a non-flaring flux density $S_{21.2\,GHz} = 1.16$ Jy[5].

3.2. Context from Bright Galaxy Surveys

Continuum surveys of optically bright galaxies like NGC 3115 have not been made with the VLA or JVLA in its A configuration at $\nu = 22$ GHz. However, at a nearby frequency, 15 GHz, the Palomar sample of galaxies with optical emission-line nuclei (Ho et al. 2003) was surveyed in the A configuration with $\theta^{15\,GHz}_{geo} = 150$ mas (Nagar et al. 2005; Saikia et al. 2018). Galaxy distances extended up to 120 Mpc so the linear resolutions were 87 pc or finer. NGC 3115 is in the defining Palomar sample but was not targeted at $\nu = 15$ GHz because it lacks optical emission lines (Ho et al. 2003; Guérou et al. 2016). NGC 3115's $S_{22\,GHz}$ and $\alpha^{22\,GHz}_{10\,GHz}$ imply $S_{15\,GHz} \sim 100\,\mu$Jy, leading to a luminosity density $L_{15\,GHz} \sim 1.1 \times 10^{18}$ W Hz^{-1}. This is about a factor

[5] https://science.nrao.edu/science/service-observing

of two below the least-luminous of the 112 emission-line nuclei detected in the $\nu = 15$ GHz survey (Nagar et al. 2005; Saikia et al. 2018).

Comparing NGC 3115 with other absorption-line nuclei may offer more insights. At $\nu = 1.5$ GHz, a Northern subset of the defining Palomar sample (Ho et al. 2003) was surveyed with e-MERLIN with $\theta^{1.5\,GHz}_{geo} = 200$ mas (Baldi et al. 2018, 2021). Again, galaxy distances extended up to 120 Mpc so the linear resolutions were 120 pc or finer. Of the 28 absorption-line nuclei targeted, 5 have point-like detections with a typical luminosity density $L_{1.5\,GHz} \sim 10^{20}$ W Hz^{-1} and 23 have luminosity densities $L_{1.5\,GHz} < (0.6-60) \times 10^{18}$ W Hz^{-1}. The upper limit on NGC 3115's luminosity density at $\nu = 1.4$ GHz (Table 1) thus seems typical for an absorption-line nucleus.

At $\nu = 5$ GHz, a Northern subset of the ATLAS^{3D} sample of ETGs (Cappellari et al. 2011) was surveyed with the JVLA in its A configuration with $\theta^{5\,GHz}_{geo} = 500$ mas (Nyland et al. 2016). Galaxy distances extended up to 42 Mpc so the linear resolutions were 100 pc or finer. The rates of point-like detections are higher among emission-line nuclei ($70/101 \sim 69\%$) than among absorption-line nuclei ($6/47 \sim 13\%$), again underscoring the importance of comparing NGC 3115 with other absorption-line nuclei. For the 41 undetected absorption-line nuclei in Atlas^{3D} galaxies, the typical constraints on their luminosity densities are $L_{5\,GHz} < (1 - 10) \times 10^{18}$ W Hz^{-1}. Thus the upper limit on NGC 3115's luminosity density at 4.9 GHz (Table 1) appears to be typical for an absorption-line nucleus.

Using the aforementioned facilities at $\nu = 1.5$-50 GHz, it would be straightforward to constrain the synchrotron spectrum of NGC 3115 with high resolutions, that is, with $\theta^\nu_{geo} < 2R_{sta} \sim 720$ mas (34 pc). The most pressing need is for high-resolution data below 10 GHz.

3.3. ADAF Model

We converted NGC 3115's broadband spectrum in Figure 3 to the νL_ν SED in Figure 4. The SED of the LLAGN has an obvious synchrotron peak near $\nu_{peak} = 9$ GHz. The LLAGN has had its extent constrained to a FWHM diameter $d_{22\,GHz} < 59$ mas (2.8 pc), appears to be isolated, and has a very low luminosity, $\nu L_\nu(22\,GHz) = 1.2 \times 10^{35}$ erg s^{-1}, only about 60 times that of Sagittarius A*. Also, the simulated gas flow tailored to NGC 3115 developed ADAF traits inside the stagnation radius $R_{sta} \sim 360$ mas (17 pc; Yao & Gan 2020).

For the above reasons, we opt to interpret Figure 4 in terms of ADAF theory (e.g., Narayan & Yi 1995a,b; Mahadevan 1997; Nemmen et al. 2014; Bandyopadhyay
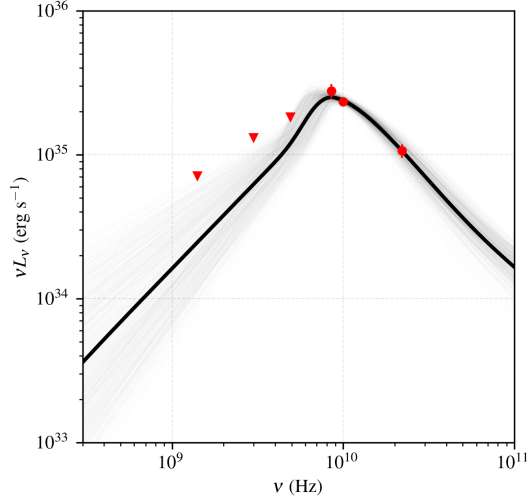
Figure 4. νL_ν SED of the LLAGN in NGC 3115, converted from Figure 3 using a distance $D = 9.7$ Mpc. The faint gray lines are individual samples from the posterior distribution, which illustrate the full range of model behavior. The thick black line shows the posterior average, which is a fit to the thermal ADAF model presented in Section 3.3.

et al. 2019; Pesce et al. 2021). In brief, ADAFs are characterized by two-temperature structures, with their ion temperatures exceeding their electron temperatures. The electrons are able to cool via a combination of synchrotron, bremsstrahlung, and inverse Compton radiation, which together define the SEDs of their emission observed across the electromagnetic spectrum. Synchrotron emission necessitates magnetic fields. These fields are typically treated as having a tangled geometry and a sub-dominant pressure that is about a tenth of the gas pressure.

Following Pesce et al. (2021), we modeled the radio SED peak in Figure 4 with a six-parameter fit to a thermal ADAF. (We included a 3σ upper limit of 2.7 mJy at $\nu = 222$ GHz (Lo et al. 2023) but that datum did not usefully constrain the model.) Table 2 gives the six parameters, their fit priors, and their fit posteriors, while Figure 5 conveys the associated corner plot. We carried out the fit using the dynesty nested sampling code (Speagle 2020). The best-constrained parameters for the ADAF are its BH mass $M_{\rm ADAF}$ and its Eddington-scaled accretion rate $\dot{M}_{\rm ADAF}/\dot{M}_{\rm Edd}$ onto the BH. We discuss all the tabulated parameters in turn below.

The BH mass $M_{\rm ADAF} = (1.2 \pm 0.2) \times 10^9 \, M_\odot$ inferred from the ADAF model agrees with previous and independent estimates of $(1-2) \times 10^9 \, M_\odot$ from stellar or hot-gas dynamics (Kormendy et al. 1996; Emsellem et al. 1999; Wong et al. 2011, 2014). The Eddington accretion rate and Schwarzschild radius associated with $M_{\rm ADAF}$
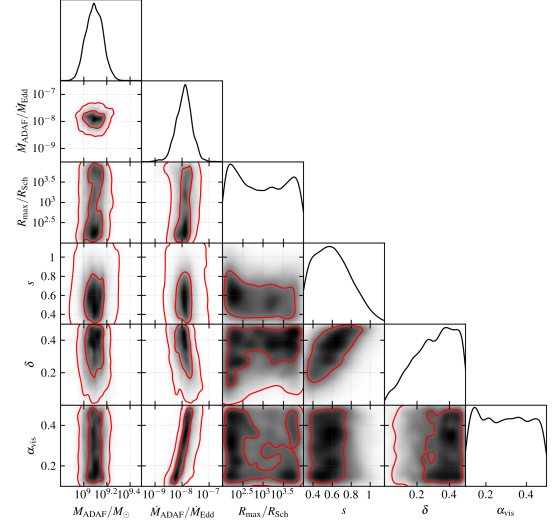
Figure 5. Posterior distributions of BH mass $M_{\rm ADAF}$, Eddington-scaled accretion rate $\dot{M}_{\rm ADAF}/\dot{M}_{\rm Edd}$, Schwarzschild-scaled maximum radius $R_{max}/R_{\rm Sch}$, power-law index for mass accretion rate versus radius s, fraction of viscous heating going directly to electrons δ, and viscosity parameter $\alpha_{\rm vis}$.

are $\dot{M}_{\rm Edd} = 26 \, M_\odot \, {\rm yr}^{-1}$ and $R_{\rm Sch} = 1.1 \times 10^{-4}$ pc, respectively.

For the LLAGN in NGC 3115, the inferred Eddington-scaled accretion rate, $\dot{M}_{\rm ADAF}/\dot{M}_{\rm Edd} = 1.2^{+1.0}_{-0.6} \times 10^{-8}$, is about 4-8 times lower than recent estimates from tailored simulations of Sagittarius A* (Event Horizon Telescope Collaboration et al. 2022a).

For an ADAF with a very low $\dot{M}_{\rm ADAF}/\dot{M}_{\rm Edd}$, Comptonization weakens and the X-ray spectrum can be dominated by bremsstrahlung emission (Yuan & Narayan 2014). Our ADAF modeling of the LLAGN in NGC 3115 indeed predicts an X-ray bremsstrahlung peak, with a 10-100 keV luminosity on the order of 10^{31} erg s^{-1} (see Figure 6). Unfortunately, the deepest X-ray search for a LLAGN in NGC 3115 involves softer wavelengths: $L_{0.5-6.0\,\rm keV} < 0.44 \times 10^{38}$ erg s^{-1} and $L_{0.5-1.0\,\rm keV} < 0.11 \times 10^{38}$ erg s^{-1} (Wong et al. 2014). At harder wavelengths, confusion from NGC 3115's population of X-ray binaries led to a limiting value of $L_{2-10\,\rm keV} < 3.9 \times 10^{38}$ erg s^{-1} for the LLAGN (Wrobel & Nyland 2012). All of these upper limits are consistent with our SED fit, which predicts that the X-ray emission from NGC 3115's LLAGN should be orders of magnitude fainter than the sensitivities achieved by the existing observations.

Optical upper limits are available but have luminosities (Almeida et al. 2018) well above the range shown in Figure 6. Future high-resolution infrared imaging (e.g., Do et al. 2014) may help improve the ADAF fitting.

Table 2. ADAF Model for NGC 3115's SED

Parameter	Description	Range of Prior	Fit Result
(1)	(2)	(3)	(4)
M_{ADAF}	BH mass	10^8-$10^{10}\,M_\odot$	$(1.2 \pm 0.2) \times 10^9\,M_\odot$
$\dot{M}_{\mathrm{ADAF}}/\dot{M}_{\mathrm{Edd}}$	Eddington-scaled accretion rate at 3 R_{Sch}	10^{-10}-10^{-5}	$1.2^{+1.0}_{-0.6} \times 10^{-8}$
$R_{\mathrm{max}}/R_{\mathrm{Sch}}$	Schwarzschild-scaled maximum radius	10^2-10^4	No significant constraint
s	Power-law index for mass accretion rate versus radius	0.3-2.0	$0.61^{+0.26}_{-0.20}$
δ	Fraction of viscous heating going directly to electrons	0.01-0.5	$0.32^{+0.12}_{-0.15}$
α_{vis}	Viscosity parameter	0.1-0.5	No significant constraint

NOTE—Three parameters are held fixed: the distance $D = 9.7\,\mathrm{Mpc}$, the canonical radiative efficiency $\eta = 0.1$, and the ratio of gas pressure to magnetic pressure $\beta = 10$.
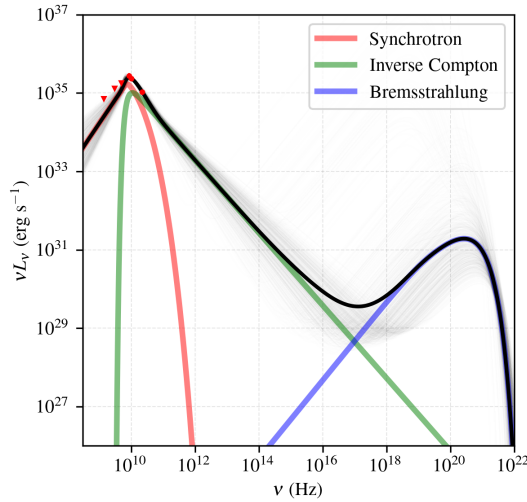
Figure 6. νL_ν SED of the LLAGN in NGC 3115, high-lighting modeled contributions from the individual emission mechanisms across the electromagnetic spectrum. Figure 4 is a zoom-in of this figure's upper-left portion.

The peak synchrotron frequency of an ADAF scales roughly as $\nu_{\mathrm{peak}} \propto M_{\mathrm{ADAF}}^{-1/2} \times (\dot{M}_{\mathrm{ADAF}}/\dot{M}_{\mathrm{Edd}})^{1/2}$ (Yuan & Narayan 2014). For the LLAGN in NGC 3115, its extreme pairing of a very high BH mass and a very low Eddington-scaled accretion rate places its synchrotron peak near $\nu_{\mathrm{peak}} = 9\,\mathrm{GHz}$, thus at radio wavelengths. This is in contrast to the oft-studied scenario of ADAFs featuring synchrotron peaks at millimeter or submillimeter wavelengths (e.g., EHT MWL Science Working Group et al. 2021; Event Horizon Telescope Collaboration et al. 2022b; Nair et al. 2024).

Other than the BH mass and accretion rate, the remaining parameters in our SED model are poorly-constrained by the available data (see Figure 5). We find a weak constraint on the power-law index for the mass accretion rate as a function of radius, $s = 0.61^{+0.26}_{-0.20}$,

which is consistent with the innermost, angle-averaged value of $s \sim 0.8$ seen in the gas flow simulation tailored to NGC 3115 (Yao & Gan 2020). We find a similarly weak constraint on the fraction of viscous heating the goes directly to electrons, $\delta = 0.32^{+0.12}_{-0.15}$. For context, early ADAF theoretical work (e.g., Narayan & Yi 1995a,b; Mahadevan 1997) typically assumed a value for δ that is roughly equal to the ratio of the electron to proton masses, that is, about 1/2000. As the theory has matured and been tested against observations, considerably larger values for δ have become favored, closer to about 0.3 (e.g., Yuan & Narayan 2014), which is consistent with our finding. Neither the maximum Schwarzschild-scaled radius $R_{\mathrm{max}}/R_{\mathrm{Sch}}$ nor the viscosity parameter α_{vis} are constrained to any significant level, and both parameters appear to be entirely prior-dominated in our fits.

The material forming NGC 3115's ADAF could affect the linear polarization of the faint radiation emerging at optically-thin frequencies $\nu > 9\,\mathrm{GHz}$ (Figure 3). Sensitive observations with the next-generation VLA (ngVLA; Murphy et al. 2018) could constrain the linear polarization at high resolutions, that is, with $\theta^\nu_{\mathrm{geo}} < 2R_{\mathrm{sta}} \sim 720\,\mathrm{mas}$ (34 pc). Detections or upper limits would guide polarization enhancements to gas flow simulations or theoretical models. Sufficiently strong polarization detections would constrain the Faraday rotation measures, enabling additional tests of simulations or models. Combined with some assumptions about the accretion flow geometry and magnetic field, rotation measures would map to accretion rates near the BH (e.g., Marrone et al. 2006; Wielgus et al. 2024).

4. BEYOND THE STAGNATION RADIUS

Gas motions were predominantly outflows beyond the stagnation radius $R_{\mathrm{sta}} \sim 360\,\mathrm{mas}$ (17 pc) identified in the simulation tailored to NGC 3115 (Yao & Gan 2020).

From hot-gas modeling, Wong et al. (2011) estimated an accretion rate $\dot{M}_{\mathrm{X-ray}} = 2.2 \times 10^{-2}\, M_{\odot}\,\mathrm{yr}^{-1}$ at the Bondi radius $R_{\mathrm{Bon}} = 3\overset{''}{.}6$ (170 pc), which is about ten times the R_{sta}. The accretion rate at the Bondi radius is thus already sub-Eddington, $\dot{M}_{\mathrm{X-ray}}/\dot{M}_{\mathrm{Edd}} = 10^{-3.1}$.

This suggests that it could be productive to seek radiative signatures, at low resolution ($\theta^{\nu}_{\mathrm{geo}} > 2R_{\mathrm{sta}}$), of material potentially being 'lost' from the outflow-dominated region. For example, deep radio continuum images could trace off-nuclear components. No off-nuclear emission has been reported from the low-resolution images in Table 1, but the RMS values of those images are quite modest (Fabbiano et al. 1989; White et al. 1997; Lacy et al. 2020). Additionally, X-ray emission lines could trace off-nuclear hot winds resembling those recently reported for M81 and NGC 7213 (e.g., Shi et al. 2021, 2022).

5. SUMMARY AND CONCLUSIONS

NGC 3115 hosts the nearest billion-solar-mass BH, with a fiducial mass $M_{\mathrm{fid}} \sim 1.5 \times 10^{9}\, M_{\odot}$ from stellar or hot-gas dynamics (Kormendy et al. 1996; Emsellem et al. 1999; Wong et al. 2011, 2014). A hydrodynamic simulation tailored to NGC 3115 found that gas motions were predominantly inflows inside the stagnation radius $R_{\mathrm{sta}} \sim 360$ mas (17 pc) and developed ADAF-like characteristics (Yao & Gan 2020). We observed the LLAGN in NGC 3115 with the JVLA at a high resolution, taken to mean $\theta^{\nu}_{\mathrm{geo}} < 2R_{\mathrm{sta}}$. This approach mitigated contamination from emission from the outflow-dominated zone beyond R_{sta}. Our principal findings are:

1. For NGC 3115, we localized a faint continuum nucleus, with flux density $S_{22\,\mathrm{GHz}} = 48.2 \pm 6.4\,\mu\mathrm{Jy}$, to a FWHM diameter $d_{22\,\mathrm{GHz}} < 59$ mas (2.8 pc). We found no evidence for adjacent emission within the stagnation radius R_{sta}. The nucleus' luminosity density $L_{22\,\mathrm{GHz}} = 5.4 \times 10^{17}\,\mathrm{W\,Hz^{-1}}$ is about 60 times that of Sagittarius A*.

2. We augmented the new $S_{22\,\mathrm{GHz}}$ with previous continuum photometry for NGC 3115 at lower radio frequencies. A detection at high resolution implied the nucleus has a spectral index $\alpha^{22\,\mathrm{GHz}}_{10\,\mathrm{GHz}} = -1.85 \pm 0.18$ ($S_{\nu} \propto \nu^{\alpha}$), indicating optically-thin synchrotron emission. Folding in upper limits at low resolution $\theta^{\nu}_{\mathrm{geo}} < 2R_{\mathrm{sta}}$, the SED of the nucleus peaks near $\nu_{\mathrm{peak}} = 9$ GHz.

3. For NGC 3115, we modeled its SED as an ADAF and inferred a BH mass $M_{\mathrm{ADAF}} = (1.2 \pm 0.2) \times 10^{9}\, M_{\odot}$, consistent with independent fiducial estimates. We also inferred an Eddington-scaled accretion rate, $\dot{M}_{\mathrm{ADAF}}/\dot{M}_{\mathrm{Edd}} = 1.2^{+1.0}_{-0.6} \times 10^{-8}$, which is about 4-8 times lower than recent estimates for Sagittarius A*.

An important next step for NGC 3115 is to conduct deep polarimetric imaging using radio facilities. This will improve the SED of the LLAGN, enable a search for very faint outflows, and constrain Faraday rotation measures to guide magnetic-field enhancements to the tailored gas-flow simulations. In addition, other absorption-line nuclei in optically bright galaxies should be searched for analogs of the LLAGN in NGC 3115. If their BHs are less massive than NGC 3115's, we speculate that their ADAFs, if present, could exhibit SEDs that peak at frequencies $\nu_{\mathrm{peak}} > 9$ GHz.

AUTHOR CONTRIBUTIONS

Author order reflects contribution effort.

Facilities: CXO - Chandra X-ray Observatory satellite, VLA - Very Large Array

Software: CARTA (Comrie et al. 2021), CASA (The CASA Team 2022), dynesty (Speagle 2020), matplotlib (Hunter 2007), numpy (van der Walt et al. 2011; Harris et al. 2020)

APPENDIX

A. SOURCE SIZE MODELING

To determine the angular size of the emitting region reported in Section 2, we fit a circularly symmetric Gaussian source structure model to the calibrated visibility data. Our model for the visibility structure $V(u, v)$ as a function of frequency ν is given by

$$V(u, v, \nu) = S \left(\frac{\nu}{22\,\text{GHz}} \right)^\alpha e^{-2\pi i (ux_0 + vy_0)} \exp \left[-2\pi^2 \sigma_G^2 (u^2 + v^2) \right], \tag{A.1}$$

where S and α are the flux density and spectral index of the source measured at $22\,\text{GHz}$, (x_0, y_0) is its coordinate location relative to the phase center of the observations, and σ_G is the Gaussian width (i.e., angular extent) of the source on the sky. These model parameters are related to the quantities reported in Section 2 by

$$S_{22\,\text{GHz}} = S \tag{A.2a}$$
$$\alpha^{26\,\text{GHz}}_{18\,\text{GHz}} = \alpha \tag{A.2b}$$
$$d_{22\,\text{GHz}} = 2\sqrt{2\ln(2)}\sigma_G. \tag{A.2c}$$

Prior to fitting, we average the calibrated data in time on 10-minute intervals and in frequency across spectral windows (64 in total, $128\,\text{MHz}$ each). For each visibility data point $\hat{V}$, our likelihood function ℓ_k is a complex Gaussian function,

$$\ell_k = \frac{1}{2\pi\sigma_k^2} \exp \left(-\frac{1}{2\sigma_k^2} \left| V(u_k, v_k, \nu_k) - \hat{V}(u_k, v_k, \nu_k) \right|^2 \right), \tag{A.3}$$

where σ_k is the uncertainty in the measurement and $V(u_k, v_k, \nu_k)$ is given by Equation A.1. We assume that the measurement uncertainty σ_k is the same for all data points, and we include this quantity as an additional parameter in our model. The total likelihood function $\mathcal{L}$ over all data points is then the product of the individual likelihoods,

$$\mathcal{L} = \prod_k \ell_k. \tag{A.4}$$

We specify uniform priors of $x_0 \sim [-0.05, 0.05]$ and $y_0 \sim [-0.05, 0.05]$ (in units of arcseconds), $S \sim [0, 100]$ (in units of mJy), $\alpha \sim [-5, 0]$, $\sigma_G \sim [0, 0.05]$ (in units of arcseconds), and $\sigma_k \sim [1, 5]$ (in units of mJy). We used the nested sampling package dynesty (Speagle 2020) to carry out the parameter space exploration, for which results are summarized in Section 2 and shown in Figure 2.

REFERENCES

Almeida, I., Nemmen, R., Wong, K.-W., Wu, Q., & Irwin, J. A. 2018, MNRAS, 475, 5398, doi: 10.1093/mnras/sty128

Baldi, R. D., Williams, D. R. A., McHardy, I. M., et al. 2018, MNRAS, 476, 3478, doi: 10.1093/mnras/sty342

—. 2021, MNRAS, 500, 4749, doi: 10.1093/mnras/staa3519

Bandyopadhyay, B., Xie, F.-G., Nagar, N. M., et al. 2019, MNRAS, 490, 4606, doi: 10.1093/mnras/stz2874

Capetti, A., Kharb, P., Axon, D. J., Merritt, D., & Baldi, R. D. 2009, AJ, 138, 1990, doi: 10.1088/0004-6256/138/6/1990

Cappellari, M., Emsellem, E., Krajnović, D., et al. 2011, MNRAS, 413, 813, doi: 10.1111/j.1365-2966.2010.18174.x

CASA Team, Bean, B., Bhatnagar, S., et al. 2022, PASP, 134, 114501, doi: 10.1088/1538-3873/ac9642

Cho, H., Prather, B. S., Narayan, R., et al. 2023, ApJL, 959, L22, doi: 10.3847/2041-8213/ad1048

Comrie, A., Wang, K.-S., Hsu, S.-C., et al. 2021, CARTA: The Cube Analysis and Rendering Tool for Astronomy, 2.0.0, Zenodo, doi: 10.5281/zenodo.4905459

Do, T., Wright, S. A., Barth, A. J., et al. 2014, AJ, 147, 93, doi: 10.1088/0004-6256/147/4/93

Doeleman, S. S., Barrett, J., Blackburn, L., et al. 2023, Galaxies, 11, 107, doi: 10.3390/galaxies11050107

EHT MWL Science Working Group, Algaba, J. C., Anczarski, J., et al. 2021, ApJL, 911, L11, doi: 10.3847/2041-8213/abef71

Emsellem, E., Dejonghe, H., & Bacon, R. 1999, MNRAS, 303, 495, doi: 10.1046/j.1365-8711.1999.02210.x

Event Horizon Telescope Collaboration, Akiyama, K., Alberdi, A., et al. 2022a, ApJL, 930, L16, doi: 10.3847/2041-8213/ac6672

—. 2022b, ApJL, 930, L13, doi: 10.3847/2041-8213/ac6675

Fabbiano, G., Gioia, I. M., & Trinchieri, G. 1989, ApJ, 347, 127, doi: 10.1086/168103

GRAVITY Collaboration, Abuter, R., Amorim, A., et al. 2019, A&A, 625, L10, doi: 10.1051/0004-6361/201935656

Guérou, A., Emsellem, E., Krajnović, D., et al. 2016, A&A, 591, A143, doi: 10.1051/0004-6361/201628743

Guo, M., Stone, J. M., Kim, C.-G., & Quataert, E. 2023, ApJ, 946, 26, doi: 10.3847/1538-4357/acb81e

Harris, C. R., Millman, K. J., van der Walt, S. J., et al. 2020, Nature, 585, 357, doi: 10.1038/s41586-020-2649-2

Heckman, T. M., & Best, P. N. 2014, ARA&A, 52, 589, doi: 10.1146/annurev-astro-081913-035722

Ho, L. C. 2008, ARA&A, 46, 475, doi: 10.1146/annurev.astro.45.051806.110546

—. 2009, ApJ, 699, 626, doi: 10.1088/0004-637X/699/1/626

Ho, L. C., Filippenko, A. V., & Sargent, W. L. W. 2003, ApJ, 583, 159, doi: 10.1086/345354

Hunter, J. D. 2007, Computing In Science & Engineering, 9, 90, doi: 10.1109/MCSE.2007.55

Inayoshi, K., Ichikawa, K., & Ho, L. C. 2020, ApJ, 894, 141, doi: 10.3847/1538-4357/ab8569

Inayoshi, K., Ostriker, J. P., Haiman, Z., & Kuiper, R. 2018, MNRAS, 476, 1412, doi: 10.1093/mnras/sty276

Johnson, M. D., Akiyama, K., Blackburn, L., et al. 2023, Galaxies, 11, 61, doi: 10.3390/galaxies11030061

Jones, M. L., Burke-Spolaor, S., Nyland, K., & Wrobel, J. M. 2019, ApJ, 874, 113, doi: 10.3847/1538-4357/ab0a09

Kormendy, J., Bender, R., Richstone, D., et al. 1996, ApJL, 459, L57, doi: 10.1086/309950

Krajnović, D., & Jaffe, W. 2002, A&A, 390, 423, doi: 10.1051/0004-6361:20020801

Lacy, M., Baum, S. A., Chandler, C. J., et al. 2020, PASP, 132, 035001, doi: 10.1088/1538-3873/ab63eb

Lo, W.-P., Asada, K., Matsushita, S., et al. 2023, ApJ, 950, 10, doi: 10.3847/1538-4357/acc855

Mahadevan, R. 1997, ApJ, 477, 585, doi: 10.1086/303727

Marrone, D. P., Moran, J. M., Zhao, J.-H., & Rao, R. 2006, ApJ, 640, 308, doi: 10.1086/500106

Murphy, E. J., Bolatto, A., Chatterjee, S., et al. 2018, in Astronomical Society of the Pacific Conference Series, Vol. 517, Science with a Next Generation Very Large Array, ed. E. Murphy, 3, doi: 10.48550/arXiv.1810.07524

Nagar, N. M., Falcke, H., & Wilson, A. S. 2005, A&A, 435, 521, doi: 10.1051/0004-6361:20042277

Nair, D. G., Nagar, N. M., Ramakrishnan, V., et al. 2024, arXiv e-prints, arXiv:2412.20276, doi: 10.48550/arXiv.2412.20276

Narayan, R., & Yi, I. 1995a, ApJ, 452, 710, doi: 10.1086/176343

—. 1995b, ApJ, 444, 231, doi: 10.1086/175599

Nemmen, R. S., Storchi-Bergmann, T., & Eracleous, M. 2014, MNRAS, 438, 2804, doi: 10.1093/mnras/stt2388

Norris, M. A., Kannappan, S. J., Forbes, D. A., et al. 2014, MNRAS, 443, 1151, doi: 10.1093/mnras/stu1186

Nyland, K., Young, L. M., Wrobel, J. M., et al. 2016, MNRAS, 458, 2221, doi: 10.1093/mnras/stw391

Perley, R. A., & Butler, B. J. 2017, ApJS, 230, 7, doi: 10.3847/1538-4365/aa6df9

Perley, R. A., Chandler, C. J., Butler, B. J., & Wrobel, J. M. 2011, ApJL, 739, L1, doi: 10.1088/2041-8205/739/1/L1

Pesce, D. W., Palumbo, D. C. M., Narayan, R., et al. 2021, ApJ, 923, 260, doi: 10.3847/1538-4357/ac2eb5

Reid, M. J., Menten, K. M., Brunthaler, A., et al. 2019, ApJ, 885, 131, doi: 10.3847/1538-4357/ab4a11

Ressler, S. M., Quataert, E., & Stone, J. M. 2018, MNRAS, 478, 3544, doi: 10.1093/mnras/sty1146

Saikia, P., Körding, E., Coppejans, D. L., et al. 2018, A&A, 616, A152, doi: 10.1051/0004-6361/201833233

Shcherbakov, R. V., Wong, K.-W., Irwin, J. A., & Reynolds, C. S. 2014, ApJ, 782, 103, doi: 10.1088/0004-637X/782/2/103

Shi, F., Li, Z., Yuan, F., & Zhu, B. 2021, Nature Astronomy, 5, 928, doi: 10.1038/s41550-021-01394-0

Shi, F., Zhu, B., Li, Z., & Yuan, F. 2022, ApJ, 926, 209, doi: 10.3847/1538-4357/ac4789

Skrutskie, M. F., Cutri, R. M., Stiening, R., et al. 2006, AJ, 131, 1163, doi: 10.1086/498708

Speagle, J. S. 2020, MNRAS, 493, 3132, doi: 10.1093/mnras/staa278

Thompson, A. R., Clark, B. G., Wade, C. M., & Napier, P. J. 1980, ApJS, 44, 151, doi: 10.1086/190688

Tonry, J. L., Dressler, A., Blakeslee, J. P., et al. 2001, ApJ, 546, 681, doi: 10.1086/318301

van der Walt, S., Colbert, S. C., & Varoquaux, G. 2011, Computing in Science and Engineering, 13, 22, doi: 10.1109/MCSE.2011.37

White, R. L., Becker, R. H., Helfand, D. J., & Gregg, M. D. 1997, ApJ, 475, 479, doi: 10.1086/303564

Wielgus, M., Issaoun, S., Martí-Vidal, I., et al. 2024, A&A, 682, A97, doi: 10.1051/0004-6361/202347772

Wong, K.-W., Irwin, J. A., Shcherbakov, R. V., et al. 2014, ApJ, 780, 9, doi: 10.1088/0004-637X/780/1/9

Wong, K.-W., Irwin, J. A., Yukita, M., et al. 2011, ApJL, 736, L23, doi: 10.1088/2041-8205/736/1/L23

Wrobel, J. M., & Nyland, K. 2012, AJ, 144, 160, doi: 10.1088/0004-6256/144/6/160

Yao, Z., & Gan, Z. 2020, MNRAS, 492, 444, doi: 10.1093/mnras/stz3474

Yuan, F., & Narayan, R. 2014, ARA&A, 52, 529, doi: 10.1146/annurev-astro-082812-141003